THE UNIVERSITY of EDINBURGH

Edinburgh Research Explorer

Seismic Performance of Pretensioned Centrifugal Spun Concrete Piles with Combined Steel Strands and Deformed Steel Bars

Citation for published version:
Ren, J, Xu, Q, Chen, G, Yu, X, Gong, S & Lu, Y 2023, 'Seismic Performance of Pretensioned Centrifugal Spun Concrete Piles with Combined Steel Strands and Deformed Steel Bars', *Journal of Structural Engineering*, vol. 149, no. 11. https://doi.org/10.1061/JSENDH.STENG-12339

Digital Object Identifier (DOI):
10.1061/JSENDH.STENG-12339

Link:
Link to publication record in Edinburgh Research Explorer

Document Version:
Peer reviewed version

Published In:
Journal of Structural Engineering

General rights
Copyright for the publications made accessible via the Edinburgh Research Explorer is retained by the author(s) and / or other copyright owners and it is a condition of accessing these publications that users recognise and abide by the legal requirements associated with these rights.

Take down policy
The University of Edinburgh has made every reasonable effort to ensure that Edinburgh Research Explorer content complies with UK legislation. If you believe that the public display of this file breaches copyright please contact openaccess@ed.ac.uk providing details, and we will remove access to the work immediately and investigate your claim.

Download date: 04. Sep. 2023

Seismic Performance of Pretensioned Centrifugal Spun Concrete Piles with Combined Steel Strands and Deformed Steel Bars

Junwei Ren[1]; Quanbiao Xu[2]; Gang Chen[3]; Xiaodong Yu[4]; Shunfeng Gong[5]; and Yong Lu, F.ASCE[6]

[1] Ph.D. Student, Dept. of Civil Engineering, Zhejiang Univ., Hangzhou 310058, China. Email: junweikid@zju.edu.cn

[2] Senior Engineer, Architectural Design & Research Institute of Zhejiang University Co. Ltd., and Research Center for Balance Architecture, Zhejiang Univ., Hangzhou 310028, China. Email: 18080397@qq.com

[3] Senior Engineer, Architectural Design & Research Institute of Zhejiang University Co. Ltd., and Research Center for Balance Architecture, Zhejiang Univ., Hangzhou 310028, China. Email: gnome@zju.edu.cn

[4] Senior Engineer, Ningbo Yizhong Concrete Pile Co. Ltd., Ningbo 315450, China. Email: jdyuxd@sina.com

[5] Professor, Dept. of Civil Engineering, Zhejiang Univ., Hangzhou 310058, China (Corresponding author). Email: sfgong@zju.edu.cn

[6] Professor, Institute for Infrastructure and Environment, School of Engineering, The Univ. of Edinburgh, Edinburgh EH9 3JL, United Kingdom. Email: yong.lu@ed.ac.uk

Abstract: Pretensioned spun high-strength concrete piles usually use the traditional helical grooved steel bars as the main reinforcement, which leads to insufficient ductility. Replacing prestressing steel bars with steel strands can effectively overcome the problem. To further enhance the overall seismic performance of the piles, pretensioned centrifugal spun concrete piles with a combined use of pretensioned steel strands and non-prestressing deformed steel bars (PSRC piles) have been developed. This paper presents the experimental and numerical investigations into the seismic performances of PSRC piles. Three full-scale PSRC pile specimens have been tested under lateral cyclic loading with different axial compressive forces, and the results are analyzed in detail and discussed. The influence of incorporating the deformed steel bars on the cyclic behavior of piles is examined with comparison to the previous test results of the counterpart piles with only steel strands. A detailed finite element model of the PSRC pile specimens is developed and verified against the test results.

Parametric analyses are then carried out using the validated model. The results show that the incorporation of non-prestressing deformed steel bars markedly improves the cracking behavior of the piles with much diffused crack distributions. The combined use of steel strands and deformed bars also results in better deformation capacity as well as higher load bearing capacity. By adjusting the concrete wall thickness and selecting a desirable ratio of prestressing steel strands and non-prestressing deformed bars, sufficient deformation and load bearing capacities can be ensured with the piles.

Author keywords: Seismic performance; Axial force ratio; Pretensioned spun concrete pile; Parametric analysis; Deformed steel bar; Steel strand

Introduction

As a widely used type of precast prestressed concrete piles (PPCPs) (Dolati and Mehrabi 2021), pretensioned spun high-strength concrete (PHC) piles are usually made of high-strength concrete and prestressing helical grooved steel bars (HGBs) through a centrifugal forming procedure. Compared with cast-in-drilled-hole (CIDH) reinforced concrete piles (Budek et al. 2000), PHC piles have remarkable advantages including efficiency in the production, good forming quality and high axial load-carrying capacity. However, HGBs used as the prestressing tendons in PHC piles have significant drawbacks including poor quality stability and severe tensile brittleness. Moreover, the pre-tensioning stresses in HGBs are often uneven due to inadequate anchoring contact between the pier heads of tendons and the anchor holes of the end plates of PHC piles. These problems generally lead to brittle failure in PHC piles under severe horizontal load or seismic load (Uzuoka et al. 2007; Wang et al. 2019). For this reason, in the medium and high intensity seismic areas, PHC piles are not commonly used for the pile heads, but rather in the lower pile sections (Thusoo et al. 2021).

In order to overcome the above problems, methods of using high-strength steel strands (HSSs) with better tensile ductility and quality stability as the prestressing tendons of spun concrete piles have been proposed by

48 this research group, as presented in Zhang et al. (2022), and piles using HSSs as the longitudinal prestressing
49 tendons, called as PSC piles, have been developed. Compared with common prestressed concrete round piles
50 and octagonal piles (Park and Falconer 1983; Budek and Priestley 2005; Silva et al. 2001), the initial pre-
51 stresses in the prestressing tendons and concrete in PSC piles are evenly distributed along the pile body due to
52 the special anchorage structure at two ends of the piles. Moreover, the relative slippage between prestressing
53 tendons and pile body concrete is extremely small, even when a large lateral deformation occurs in the pile
54 body. Results from the flexural test of PSC piles (Zhang et al. 2022) demonstrated that PSC piles with a smaller
55 amount of prestressing tendons showed better deformation capacity as well as higher bearing capacity than
56 PHC piles.

57 Despite the above improvements, PSC piles still exhibited an undesirable cracking behavior, which was
58 similar to that of PHC piles. The crack pattern was characterized by a small number of cracks with a large
59 crack width on average. Such a crack pattern usually results in high strain concentration, which can lead to
60 premature tensile rupture of longitudinal reinforcements at the main crack in the case of tension-bending failure.
61 In general, the crack width tends to reduce as the longitudinal reinforcement ratio decreases. But the number
62 of prestressing tendons in pretensioned spun concrete piles is generally governed by the initial pre-stress
63 requirements (GT 2020), and this means that the scope of facilitating further improvement of seismic
64 performances would be limited for piles using prestressing tendons alone. Therefore, the concept of a mixed
65 use of non-prestressing deformed steel bars in PSC piles was envisaged to improve the cracking behavior as
66 well as the overall seismic performances. Accordingly, pretensioned spun concrete piles using combined steel
67 strands and deformed steel bars as longitudinal reinforcements, called PSRC piles, have been developed. The
68 incorporation of deformed steel bars to the piles affects little the initial pre-stress state of prestressing tendons
69 and concrete, but helps improve the cracking behavior, and at the same time increases the seismic load carrying

70 capacity of the piles due to an increase of the total longitudinal reinforcement ratio.

71 A preliminary experimental study of the developed PSRC piles under bending (Ren et al. 2021) has found
72 that the concrete cracking pattern of PSRC piles was indeed significantly improved, with a denser distribution
73 of cracks and a smaller crack width. To fully understand the influence of the mixed use of non-prestressing
74 deformed steel bars on the seismic behavior of the PSRC piles, cyclic loading tests with the presence of axial
75 force need to be conducted.

76 In terms of the behavior of piles under cyclic loading, extensive research has been focused on PHC piles
77 subjected to cyclic loads. Nagae and Hayashi (2003) performed seismic experiments of PHC piles designed
78 with an effective loading height-to-diameter ratio (H/D) of 3 and found that the effect of lateral reinforcement
79 ratio on the deformation capacity of piles was related to the axial load. Yang et al. (2018) designed a set of
80 three-point loading test setup to assess the cyclic performances of PHC piles with H/D of 3.5-5.5 under cyclic
81 loading, and the results indicated that brittle failure occurred and this was caused by the rupture of prestressing
82 steel bars. Zhang et al. (2020) carried out full-scale seismic experiments on PHC piles with H/D of about 3
83 subjected to combined cyclic loads and an axial force, and it was found that the axial force significantly
84 affected the damage mode of piles. The tests of PHC piles conducted by Huang et al. (2018) using model pile
85 specimens demonstrated that bending damage mainly occurred in the piles, and the maximum moment and
86 damage were mainly concentrated at an embedded depth of $4D$ to $6D$. In general, the bending-dominated
87 failure mode is expected in piles or columns with H/D larger than 3 (Tong et al. 2019). Therefore, to realistically
88 replicate the possible structural behavior and failure mode, piles with a large effective height to diameter ratio
89 (H/D), such as 4 to 6, should be investigated (Ren et al. 2022). Moreover, the presence of axial force needs to
90 be taken into consideration because a varying axial force will exist in piles as a consequence of the vertical
91 loads of the superstructures, which will considerably affect the structural performance of the piles (Joen and

92 Park 1990; Roeder et al. 2005).

93 The role of the axial force on the seismic performance of PSRC piles has not been investigated
94 systematically in previous research. The structural behavior and failure mode of PSRC piles with a large
95 height-to-diameter ratio of 4 to 6 are also not fully understood under combined lateral cyclic loading and axial
96 force. Furthermore, due to limited experimental data, improved numerical simulation will be of significant
97 benefit for an assessment of key design factors. In this paper, the cyclic loading tests on three full-scale PSRC
98 pile specimens with a large height-to-diameter of about 6 and under low, medium and high axial compressive
99 forces, as commonly encountered in engineering practice, are presented. The effect of incorporating deformed
100 steel bars on the cyclic behavior of the piles is analyzed with comparison to the previous test results of the
101 counterpart piles with only steel strands. A dedicated three-dimensional finite element (FE) model is developed
102 using a novel modeling method in DIANA (TNO 2020) to predict the seismic responses of PSRC piles. Using
103 the validated FE model, parametric analysis is performed to explore the effects of prestressing level of steel
104 strands, prestressing tendon ratio, non-prestressing rebar ratio and concrete wall thickness on the seismic
105 performances of PSRC piles.

106 **Experimental program**

107 *Design consideration of PSRC piles*

108 In the design of PSRC piles with a combination of prestressing strands and normal deformed steel bars, the
109 amount of the prestressing strands was kept the same as the PSC piles (without deformed steel bars) so that
110 the level of prestress in the concrete remains essentially the same under the same level of control prestressing
111 force in the strands. On this basis, deformed steel bars were added and the number of the deformed steel bars
112 was made to match that of the steel strands so as to prevent any adverse effects of asymmetric reinforcement
113 in the circular section on the prestressing process and the structural performance of the piles. Thus, eleven

deformed steel bars were arranged evenly along the distribution circle of longitudinal tendons together with the steel strands. According to the preliminary analysis, a deformed steel bar ratio ranging from 1% to 2% tends to be reasonable for this type of hybrid reinforced piles, and this led to the choice of 16-mm diameter deformed steel bars for the PSRC pile specimens.

Test specimens

A representative PSRC pile was designed in accordance with the specification commonly used in engineering practice in China (GT 2020). The cross section was selected to have a diameter D of 500 mm and a wall thickness of 100 mm. The effective loading height H was 2900 mm, giving rise a H/D ratio about 6.

Three identical PSRC pile specimens, namely PSRC-1, PSRC-2 and PSRC-3, were constructed for testing under three different axial compressive forces, respectively. The geometry and dimensions of the test piles are shown in Fig. 1. The footing and cap were heavily reinforced and had sufficient flexural and shear strengths to ensure that they remain intact during the test.

Table 1 and Fig. 2 present detailed reinforcement arrangements of PSRC piles. The prestressing tendons used in the piles were high-strength 7-wire steel strands (HSS). Hot-rolled ribbed bars (HRB), i.e., deformed steel bars, were used for the non-prestressing tendons. Cold-rolled ribbed bars (CRB) with improved elongation capacity were used for the stirrups. The nominal tensile strength f_{ptk} for HSSs was 1860 MPa and the pre-tensioning control stress σ_{con} was 1302 MPa, giving a prestressing level of 70%.

The design axial force ratio, i.e., P/Af_{cd}, was 0, 0.2 and 0.4 for the three PSRC pile specimens, respectively. The corresponding axial compressive force P was calculated according to the design concrete strength f_{cd}, which was 39.9 MPa for C90 concrete (GT 2020), and the pile cross-sectional area A, to be 0, 1003 kN and 2006 kN, respectively.

Grade C90 high-strength concrete was used for PSRC piles. The actual axial compressive strength f_c of the

concrete was estimated to be 74.7 MPa (Ren et al. 2022), and this strength will be employed later for modeling the actual concrete behavior in the FE simulation. For the reinforcement, three samples were tested for each type of steel bars, namely a) Φ^{S}11.1 HSS, b) D16 HRB and c) Φ^{RH}5 CRB, to obtain material mechanical properties. Table 2 summarizes the average mechanical parameters, where E_s is the elastic modulus, f_y is the yield strength, f_u is the ultimate strength, and A_{gt} is the maximum elongation.

Test setup and loading scheme

The test setup is illustrated in Fig. 3. The specimens were subjected to lateral cyclic loading by an MTS actuator, which was horizontally fixed on the reaction wall and connected to the pile body at 2900 mm height above the footing. The vertical forces were applied on the specimen top through a hydraulic jack and a special hinge support, which enables the specimen to rotate freely at the top, avoiding unwanted bending moment at this position. A special rolling device was designed and installed between the reaction steel girder and the jack to minimize the friction force, thereby ensuring the smooth movement of the specimen top. As marked in Fig. 3(a), four displacement transducers, labeled as H1 to H4, were installed to measure the deformation responses of specimens; H1 and H2 for measuring the horizontal displacements of the loading points, and H3 and H4 for measuring the displacements of the footing to monitor any slippage or rotation at the fixed footing. A series of strain gauges were installed on the concrete surface along the pile body to monitor the key concrete strains.

The specific lateral cyclic loading protocol consisted of a force-controlled stage with one cycle for each loading step and a displacement-controlled stage with three repeated cycles for each displacement level (Wang et al. 2022). An increment of 20 kN was applied to the specimen at the first stage until the force was near the estimated yield load of the specimen (GT 2020). A nominal yield displacement Δ_y was determined according to the apparent nonlinear characteristics of the test hysteretic curve. Based on the obtained Δ_y, the loading was switched to the displacement-controlled stage with an increment of displacement Δ_0 = 10 mm. The test was

158 terminated when the bending moment capacity of the specimens reduced to 80% of the maximum value.

159 **Experimental process and general observations**

160 *Specimen PSRC-1*

161 For the specimen PSRC-1 under a zero axial force, the concrete crack first appeared near the pile bottom at
162 ±80 kN force level. When the loading reached ±120 kN, apparent nonlinear characteristics were observed from
163 the hysteretic curve, indicating that the specimen entered into the yield state. At this point, the loading was
164 switched to a displacement-controlled mode with a nominal Δ_y equal to ±25 mm (±0.86% drift). In subsequent
165 displacement loading cycles, the cracks on both sides of the specimen continued to propagate along the
166 horizontal circumferential direction. The specimen PSRC-1 attained the peak strengths at a displacement of
167 ±85 mm (±2.93% drift) for both loading directions. Meanwhile, the cover concrete in the pile bottom began to
168 crush, and the damage region expanded as the displacement further increased. The reinforcing bars were
169 exposed at this stage and the non-prestressing rebars (HRBs) exhibited apparent outward buckling at the pile
170 bottom under compression. When the displacement reached levels of +155 mm and −165 mm (+5.34% and
171 −5.69% drift), respectively, the stirrups (CRBs) ruptured on both sides in the bottom critical region. Towards
172 a displacement level of ±175 mm (±6.03% drift), the residual bending moments in both directions reduced to
173 below 80% of the maximum values.

174 Fig. 4 shows the failure patterns of PSRC-1. The number of main cracks was 11 on each side and the
175 distribution range of cracks was approximately 1490 mm (3.0*D*), giving an average crack spacing of 135 mm.
176 Moreover, the damage region of concrete was concentrated within a height of 200 mm (0.4*D*) at the pile bottom.
177 Overall, a flexure-dominated failure occurred in the specimen PSRC-1.

178 *Specimen PSRC-2*

179 For the specimen PSRC-2 under an axial load ratio of 0.2, the concrete cracks first appeared at force levels

of +100 kN and −120 kN in the two directions, respectively. The specimen started to show an apparent nonlinear behavior at ±160 kN force level and Δ_y was estimated to be about ±25 mm (±0.86% drift). At a displacement level of ±55 mm (±1.90% drift), the specimen attained the maximum bearing capacity and the cover concrete spalled and crushed at the same time. Towards a displacement level of ±115 mm (±3.97% drift), the damage of concrete at the pile bottom was severe, and the exposed non-prestressing rebars (HRBs) exhibited outward buckling while the prestressing tendons (HSSs) became loose under compression. The stirrups (CRBs) on the south side ruptured when the displacement level was +125 mm (+4.31% drift). The specimen finally attained a displacement level of ±135 mm (±4.66% drift).

As shown in Fig. 5, similar to PSRC-1, the specimen PSRC-2 had 11 main cracks on each side, distributed in a range of 1410 mm (2.8*D*), giving an average spacing of 128 mm. The damage height of concrete was 370 mm (0.7*D*) for PSRC-2, which was larger than that of PSRC-1. The specimen PSRC-2 also suffered the flexure-dominated failure.

Specimen PSRC-3

For specimen PSRC-3 under a high axial load ratio of 0.4, the concrete cracks began to appear at ±120 kN force level. The specimen entered into the yielding state at ±180 kN force level, and Δ_y was estimated to be about ±20 mm (±0.69% drift), which was smaller than that of PSRC-1 and PSRC-2. The specimen PSRC-3 reached the maximum bearing capacity at a displacement level of ±50 mm (±1.72% drift). The subsequent load cycles were accompanied by spalling and crushing of concrete, outward buckling of non-prestressing rebars (HRBs) and loosening of prestressing tendons (HSSs). At a displacement level of ±90 mm (±3.10% drift), the stirrups (CRBs) ruptured on both sides of the specimen as the buckled rebars pushed outward.

The specimen PSRC-3 again exhibited a flexure-dominated failure mode. The crack pattern was similar to that of specimens PSRC-1 and PSRC-2, with also 11 main cracks as shown in Fig. 6. The distribution range of

202 cracks was 1360 mm (2.7*D*) and the average spacing was 124 mm. The damage of concrete covered a height
203 of 600 mm (1.2*D*), which was notably larger than the other two specimens.

204 **Detailed experimental results and analysis**

205 *Hysteretic curves*

206 Fig. 7(a), (c) and (e) show the lateral force-displacement (*F*-*S*) hysteretic curves of the three specimens. The
207 hysteretic hoops appeared to be bow-shaped, showing a notable degree of pinching effect. This is because the
208 prestressing tendons (HSSs) in the pile specimens were mainly in tension and contributed less in compression
209 during cyclic loading, so that the specimens had a certain self-centering capacity. To analyze the actual load-
210 carrying capacity of these specimens and enable a better comparison among them, the bending moment at the
211 pile bottom cross-section is re-produced taking into account the secondary moment caused by the *P*-Δ effect.
212 The bending moment is then plotted against the drift (*M*-θ curves) in Fig. 7(b), (d) and (f).

213 *Backbone curves*

214 Fig. 8 illustrates the *M*-θ backbone curves of the three PSRC pile specimens. The yield point is determined
215 according to the secant line at 75%M_{max}. The ultimate point, which indicates the specimen failure, is defined
216 when the post-peak bending moment capacity drops to 80%M_{max} (Germano et al. 2016).

217 Four distinct stress stages can be observed from the backbone curves, including elastic stage, elastic-plastic
218 stage, plastic stage and failure stage. In the first stage, the specimens remained quasi-elastic until the point
219 when cracks began to occur. In the elastic-plastic stage, i.e., from the crack point to the yield point, the length,
220 width and number of concrete cracks further developed, while the reinforcements remained elastic until the
221 yield point. During the plastic stage, the overall specimens showed apparent nonlinearity and the strength
222 reached the maximum at the peak point. After that, the specimens exhibited a gradual decrease in post-peak
223 strength in the failure stage. The descending rate accelerated as the axial compressive force increased. At the

224 ultimate point, the specimens lost most of their bearing capacity due to concrete crushing and stirrup rupture.

225 The main seismic behavioral parameters obtained from the experiments are summarized in Table 3. The
226 ductility factor μ_θ is taken as the ratio of the ultimate drift θ_u to the yield drift θ_y. It can be observed that the
227 strengths and deformations of the specimens at each response stage were significantly affected by the axial
228 compressive force. The bending moments at each key point increased as the axial force ratio increased. For
229 instance, the peak moment M_{max} of PSRC-3 was 53.7% larger than that of PSRC-1. On the other hand, however,
230 the ultimate drift θ_u and the ductility factor μ_θ decreased with the increase of the axial compression force. It is
231 worth noting that μ_θ of all specimens are larger than 3, which is a reasonable design value for the ductility
232 factor of pile foundations (Ren et al. 2022). The specimens are deemed to conform to the displacement-based
233 design requirement of a typical ultimate drift of 3% for piles or columns (Kowalsky et al. 1995). It shows that
234 PSRC piles exhibit adequate ductility under low, medium and high axial force ratios.

235 *Stiffness degradation and energy dissipation*

236 Fig. 9(a) illustrates the normalized stiffness degradation curves of the three PSRC pile specimens. The secant
237 stiffness K_i is the ratio of the moment M to the corresponding drift θ at each loading level. The effective
238 stiffness K_e is derived in accordance with the guideline FEMA 356 (2000), with values of 72.7×10^3 kN·m/rad,
239 101.1×10^3 kN·m/rad and 127.5×10^3 kN·m/rad for specimens PSRC-1, PSRC-2 and PSRC-3, respectively.
240 It can be observed that the stiffness of all PSRC pile specimens decreased rapidly before the yield point, but
241 the rate of decrease slowed down afterwards. When the deformation response was large, a higher axial
242 compressive force would tend to accelerate the descending rate of the stiffness due to the P-Δ effect.

243 The equivalent viscous damping ratio ζ_{eq} is used to evaluate the relative energy dissipation capacity of PSRC
244 pile specimens, and the results are shown in Fig. 9(b). Before the yield point, ζ_{eq} of the specimens decreased
245 as the deformation response increased. ζ_{eq} then showed an upward trend after the yielding of the specimens,

246 and this was mainly resulted from the obvious plastic deformation response of longitudinal tendons in tension
247 and nonlinear characteristics of concrete in compression. The values of ζ_{eq} of all three specimens were
248 concentrated in the range of 10%-15% after yielding, which is comparable to standard designed piles or
249 columns with a solid cross section (Kowalsky et al. 1995).

250 **Comparison between PSRC piles and PSC piles**

251 The authors (Ren et al. 2023) have previously conducted the seismic experiments of three PSC pile
252 specimens with the same design as the PSRC pile specimens presented herein. However, in the PSC piles only
253 prestressing tendon HSSs were used as the longitudinal reinforcement, as shown in Table 1. For PSC piles, the
254 prestressing tendon ratio has upper and lower limits to ensure that the compressive pre-stress of concrete is
255 within an appropriate range of 5 MPa to 10 MPa (GT 2020), which should meet both the requirements of
256 sufficient crack resistance and vertical load bearing capacity. Thus, the prestressing tendon ratio of the
257 specified pile type should remain more or less the same, and for this reason it was necessary to add deformed
258 bars in the design of the PSRC piles, while keeping the amount and configuration of the prestressing strands,
259 to explore the improvement of the overall structural performance of the piles.

260 The *F*-*S* hysteretic curves of three PSC pile specimens are shown in Fig. 10(a), (b) and (c). Comparing with
261 those shown in Fig. 7, it can be observed that under the same axial force ratio (P/Af_{cd}), the pinching effect of
262 the hysteretic curves for the PSRC pile specimens was markedly improved as compared with the PSC pile
263 specimens. This can be attributed to the involvement of the non-prestressing deformed bars (HRBs), in that
264 these reinforcing bars underwent sufficient tension-compression deformation cycles during the cyclic loading,
265 which alleviated the self-centering effect of the specimens due to the prestressing tendons and increased the
266 fullness of the hysteretic curves.

267 The test results of three PSC pile specimens showed that the average number of concrete cracks in the pile

body was 5, 5 and 6 under an axial force ratio of 0, 0.2 and 0.4, with crack spacing of 220 mm, 208 mm and 150 mm, respectively. Compared with PSC piles, PSRC piles exhibited a markedly enhanced crack pattern with a smaller spacing as a result of the incorporation of non-prestressing rebar HRBs, which increased the bond between concrete and the longitudinal reinforcement overall. The presence of HRBs also improved the condition of the concrete in the compression zone in the critical region, which in turn enhanced the structural resistance of the piles.

For the PSC pile specimen under a zero axial force ratio, the final failure was the rupture of critical prestressing tendon HSSs, which was caused by the highly concentrated deformation at the main concrete crack with a large width. This situation was prevented in the PSRC pile specimen due to better distributed cracks with relatively small widths benefitting from the incorporation of HRBs. For the pile specimens under 0.2 and 0.4 axial force ratios, the final failure modes of the two types of piles were similar; however, due to the different configurations of longitudinal reinforcements, the seismic behavioral parameters between each pair of piles were different.

Fig. 11 shows the backbone curves of M-θ for the PSRC and PSC pile specimens. As listed in Table 3, the peak moments of PSRC piles were markedly larger than those of PSC piles under the same axial force ratio, indicating that the incorporation of non-prestressing HRBs in the piles can significantly improve their load-carrying capacity. For piles under a zero axial force ratio, the ultimate drift of PSRC pile was 35.2% larger than that of PSC pile. For the cases of 0.2 and 0.4 axial force ratios, the ultimate drifts, as well as ductility factors, of PSRC piles were also larger comparing to their counterpart PSC piles.

For piles under medium and high axial compressive forces, the post-peak strength degradation was mainly caused by the concrete crushing in the compressive region. As mentioned above, the presence of non-prestressing deformed rebar HRBs enabled a more uniform stress distribution in concrete, which reduced the

degree of local damage in the concrete under compression, and therefore improved the descending trend of the bearing capacity and improved the effective deformation capacity of piles.

Finite element analysis

Description of the FE model

Fig. 12 illustrates the FE model of PSRC pile specimens. The model encompasses all pertinent parts of the test specimens, including the concrete cap and footing, the pile, details of the reinforcement, and the steel end plate and steel bracket. 8-node solid brick element (HX24L) is adopted to model the concrete blocks and steel parts. The longitudinal reinforcing bars are modeled as bond-slip bars while stirrups are modeled as embedded bars (Tao et al. 2021). The footing of the specimen is fixed in three translational directions. Based on a mesh convergence analysis (Ren et al. 2022), the pile body is meshed by 22 divisions along the circumferential direction, 4 layers through the thickness, and 50-mm grid in the height direction. For the other components, 25 mm to 100 mm mesh is adopted according to the geometry. The total number of brick elements is 16173 and a 2×2×2 integration scheme is applied to each element, and the number of nodes is 24891.

The loads are applied by three steps: a) applying prestressing forces of longitudinal steel strands, b) applying an axial force on the pile body through the upper concrete cap, and c) applying lateral cyclic loads of test specimens via the steel bracket. In order to simulate the prestressing process accurately and consider the bond-slip effect between steel strands and concrete, tying is used to simulate the anchorage structure by connecting the head nodes of the steel strands and the corresponding nodes of the end plates within the framework of DIANA, as shown in Fig. 12. Specific implementation process is described in Ren et al. (2022).

It is worth noting that a reduced integration scheme has the advantage of a generally low computational cost, which is beneficial for large-scale computations (Nascimbene et al. 2022). But by default, DIANA performs a regular integration scheme for most types of meshes and analyses, and this integration scheme is chosen in the

present model. In order to balance computational efficiency and solution accuracy, the FE analysis with one cycle per amplitude level is performed. The average computational time for each complete analysis with the present model is about 20 hours, which is considered acceptable.

Material models

The total strain crack model in DIANA is applied for the constitutive framework of concrete, which has been shown to be robust and stable when simulating reinforced concrete structures (Nascimbene et al. 2021). The Maekawa-Fukuura compressive model, as shown in Fig. 13(a), is adopted for the compressive behavior of high-strength concrete (Lai and Liew 2021). The tensile behavior of the concrete is described by the tension softening model suggested by JSCE (2010), as depicted in Fig. 13(b). Menegotto-Pinto model (Menegotto and Pinto 1973) is applied to model the hysteretic behavior of the steel reinforcement, as shown in Fig. 13(c). The values of hardening ratio $b = E_s/E_h$ for HSSs, HRBs and CRBs are 0.020, 0.004 and 0.003, respectively.

In this FE model, the bond-slip effect between the longitudinal reinforcement and concrete is simulated on the basis of the cubic model proposed by Dörr (1980), as shown in Fig. 13(d). This bond-slip model neglects softening and assumes a yield plateau. The unloading and reloading paths of the model follow the elastic stiffness, and the envelope bond stress-slip curve is recaptured at the point where unloading occurs. Although the bond deterioration is not considered in the bond-slip model, the simulation accuracy and reliability of this model as a whole has been verified in previous studies (Ren et al. 2022; Ren et al. 2023). Other symbolic definitions and specific values of the above models can be found from Ren et al. (2022).

Validation of the FE model

Fig. 14 shows the crack patterns at the peak loading point predicted by the FE simulations as compared to the test results. It can be seen that the distribution range and number of concrete cracks along the pile body obtained by the FE models match well with the test specimens.

334 The numerical and experimental lateral load-lateral displacement hysteretic curves of three PSRC pile
335 specimens are presented in Fig. 7. The predicted results are in good agreement with the test data, including the
336 lateral forces, loading/reloading stiffness, and pinching response. The predicted values of the mean peak forces
337 for PSRC-1, PSRC-2 and PSRC-3 are 175.0 kN, 213.0 kN and 239.2 kN, and the test values are 178.0 kN,
338 205.3 kN and 231.7 kN, showing the corresponding errors of -1.7%, 3.8% and 3.3%, respectively. For the
339 reinforced concrete structures, such errors are acceptable considering many uncertainties in the tests.

340 **Parametric analysis**

341 Using the validated FE model, parametric analyses are conducted to explore the effects of the prestressing
342 level of prestressing tendon HSSs, prestressing tendon HSS ratio, non-prestressing rebar HRB ratio and
343 concrete wall thickness on the seismic behavior of PSRC piles. The model for the specimen PSRC-2 is selected
344 as a benchmark.

345 *Prestressing level of prestressing tendon HSSs*

346 The M-θ backbone curves of the models with the prestressing levels of 35%, 50% and 70% for the
347 prestressing tendon HSSs are shown in Fig. 15. It shows that the decrease in prestressing level has little effect
348 on the peak strength of PSRC piles. The ultimate deformation capacity, on the other hand, increases by 28.4%
349 with the decrease of the prestressing level from 70% to 35%. This is understandable as the initial concrete pre-
350 stress is relatively small using a lower prestressing level, thus reducing the degree of compression damage of
351 concrete under the same deformation response for piles. However, the cracking resistance of PSRC piles with
352 a low prestressing level would not be satisfactory and therefore it is not the usual practice of using a low
353 prestressing level.

354 *Prestressing tendon HSS ratio*

355 The reinforcement ratio influences the bar diameter and clear bar spacing, which may affect the bond-slip

356 relationship between the concrete and the steel bars, thus affecting the global response of the FE model.
357 However, according to the findings in Eligehausen et al. (1983), for the bar diameters and clear bar spacings
358 considered in this parametric analysis, the possible variation of the effects on the bond behavior is relatively
359 small, and therefore can be disregarded in terms of the bond-slip relationship.

360 The ratio of prestressing tendon HSSs controls the initial pre-stress of pile concrete and thus affects the
361 characteristic behavior of concrete. Three PSRC pile models with the same number and layout of HSSs but in
362 diameters of 11.1 mm, 12.7 mm and 15.2 mm are selected according to the standard (GT 2020). The
363 corresponding HSS ratios are 0.65%, 0.86% and 1.23%, and the standard initial pre-stresses for concrete are
364 6.07 MPa, 7.96 MPa and 11.04 MPa, respectively. Fig. 16 illustrates the M-θ backbone curves of the above FE
365 models. As the prestressing tendon HSS ratio increases from 0.65% to 0.86% and 1.23%, the peak strength of
366 the pile increases by 8.5% and 20.1%, but the ultimate deformation decreases sharply by 26.0% and 38.4%.
367 This indicates that excessive prestressing tendons increase the concrete compressive pre-stress, which will lead
368 to the premature crushing of concrete, and accelerate the downward trend of the bearing capacity of piles after
369 reaching the peak resistance.

370 In view of the fact that the tested PSRC piles in this study follow the standard specifications commonly used
371 in construction, from the experimental results shown in Table 3, an ultimate drift of about 4% can be
372 recommended as the standard limit state for PSRC piles under an axial force ratio of 0.2. Among the above
373 three piles with different HSS details, the PSRC pile with prestressing tendon HSSs in a diameter of 11.1 mm
374 and a relatively small ratio of 0.65% is deemed to be the best choice to ensure sufficient deformation capacity.

375 *Non-prestressing rebar HRB ratio*

376 To examine the effect of non-prestressing rebar HRB ratio on the cyclic response of PSRC piles, the PSRC
377 pile models without HRBs and with HRBs in diameters of 12 mm, 14 mm, 16 mm and 20 mm, respectively,

are analyzed. The corresponding non-prestressing HRB ratios are 0, 0.99%, 1.35%, 1.76% and 2.75%, respectively. The M-θ backbone curves of the above models are shown in Fig. 17(a). It is found that the peak strength will increase with the increase of non-prestressing HRB ratio, while the ultimate deformation tends to first increase and then decrease, as plotted in Fig. 17(b). The reduction of deformation capacity may be due to the case being over-reinforced, causing the severe damage in concrete and thus a poorer overall performance. For the particular analysis results considered herein, according to the standard limit state of an ultimate drift of 4%, the piles with non-prestressing tendon HRB ratio ranging from 0.7% to 2.2% (or in diameters from 12 mm to 16 mm) meet the displacement demands. Moreover, when the bearing capacity of piles needs to be improved, the piles with a larger non-prestressing tendon HRB ratio may be a better option.

Concrete wall thickness

The concrete wall thickness may be a key design parameter for PSRC piles as it will affect the prestressing tendon HSS ratio and the corresponding initial pre-stress of pile body concrete. The influence of the concrete wall thickness on the cyclic response of PSRC piles is analyzed based on the pile models with the same number and layout of HSSs but in diameters of 11.1 mm, 12.7 mm and 15.2 mm. Two common wall thicknesses, namely, 100 mm and 125 mm, are selected according to the standard (GT 2020). The corresponding HSS ratios are 0.65%, 0.86%, 1.23% (100 mm group) and 0.55%, 0.74%, 1.05% (125 mm group), respectively. Notably, the external axial force is adjusted according to the section areas of PSRC piles to keep the same axial force ratio (P/Af_{cd}) between two cases of wall thickness.

The M-θ backbone curves of the above models are shown in Fig. 18(a), and Fig. 18(b) illustrates the variation trends of ultimate drift vs. steel strand diameter for the above cases. It can be observed that the ultimate deformation capacity of the above piles increases by 27.4%, 21.5% and 13.0% with increasing the wall thickness, respectively. This may be explained by the fact that increasing the wall thickness results in a lower

400 prestressing tendon HSS ratio and a correspondingly lower pre-stress for concrete, which delays the damage
401 process of concrete and improves the deformation capacity of the piles. Besides, the deformation capacity of
402 the PSRC piles in all thickness cases can meet the limit drift requirement of 4% when the prestressing tendon
403 ratio is below 0.70%.

404 **Conclusions**

405 A comprehensive experimental and numerical study has been conducted to investigate the seismic behavior
406 of pretensioned spun high strength concrete piles with a combined reinforcement of high-strength high-
407 deformability steel strands (HSSs) and deformed steel bars (HRBs), called PSRC piles, with a particular
408 interest in the effects of the mixed reinforcement on the cracking and deformation performances. Based on
409 these investigations, the following conclusions can be drawn:

410 1. All three PSRC pile test specimens exhibited the flexure-dominated failure. The main failure mode of the
411 specimens was characterized by crushing of the concrete at the pile bottom and buckling of the non-
412 prestressing rebar HRBs, while the prestressing tendon HSSs became loose under compression.
413 Eventually rupture of stirrups also occurred due to a combined effect of expansion of core concrete in the
414 compression zone and outward pushing by the buckled HRBs and loosened HSSs.
415 2. The bearing capacity of PSRC piles increased with the increase of the axial force ratio while the
416 deformation capacity decreased. However, the ductility factors of all three specimens were larger than 3,
417 meeting the design requirements of the pile foundation.
418 3. Compared with PSC piles (without deformed rebar), the crack pattern of PSRC piles is markedly
419 improved due to the presence of non-prestressing deformed bar HRBs, with a wider cracking region, and
420 smaller spacing and crack width. Due to the incorporation of the HRBs, the PSRC piles exhibited greater
421 bearing capacity than PSC piles. The deformation capacity of PSRC piles also improved, and this was

attributable to improved stress distribution characteristics of concrete and a delay in the descending trend of post-peak strength of piles due to the incorporation of the HRBs. Moreover, the hysteretic curves of PSRC piles are exhibited noticeable improvement with an increased energy dissipation capacity due to the tension-compression deformation response of HRBs.

4. The proposed FE model can well predict the hysteretic behavior, bearing capacity and crack patterns of PSRC piles. Parametric analyses indicate that increasing the prestressing tendon HSS ratio and non-prestressing rebar HRB ratio can both improve the bearing capacity, but the deformation capacity of piles tends to be reduced correspondingly. According to the typical displacement-based limit state for piles, a combination of prestressing tendon HSSs with a ratio up to 0.65% and non-prestressing rebar HRBs with a ratio ranging from 0.7% to 2.2% in PSRC piles can be considered suitable for applications. Further, increasing the concrete wall thickness will generally improve the performance of the piles.

Data availability statement

Some or all data, models, or code that support the findings of this study are available from the corresponding author upon reasonable request.

Acknowledgement

The authors acknowledge the financial supports from the National Natural Science Foundation of China (Grant number: 52071290).

References

Budek, A. M., M. J. N. Priestley, and G. Benzoni. 2000. “Inelastic seismic response of bridge drilled-shaft RC pile/columns.” *Journal of Structural Engineering* 126(4): 510-517. https://doi.org/10.1061/(ASCE)0733-9445(2000)126:4(510).

Budek, A. M., and M. J. N. Priestley. 2005. “Experimental analysis of flexural hinging in hollow marine

444 prestressed pile shafts." *Coastal Engineering Journal* 47: 1-20.
445 https://doi.org/10.1142/S0578563405001161.
446 Dolati, S. S. K., and A. Mehrabi. 2021. "Review of available systems and materials for splicing prestressed-
447 precast concrete piles." *Structures* 30: 850-865. https://doi.org/10.1016/j.istruc.2021.01.029.
448 Dörr, K. 1980. "Ein beitrag zur berechnung von stahlbetonscheiben unter besonderer berücksichtigung des
449 verbundverhaltens." Ph.D. thesis, Darmstadt University, Germany.
450 Eligehausen, R., E. P. Popov, and V. V. Bertero. 1983. "Local bond stress-slip relationships of deformed bars
451 under generalized excitations." Berkeley: EERC, University of California.
452 FEMA. 2000. *Prestandard and commentary for the seismic rehabilitation of buildings*. FEMA 356.
453 Washington, DC.
454 Germano, F., G. Tiberti, and G. Plizzari. 2016. "Experimental behavior of SFRC columns under uniaxial and
455 biaxial cyclic loads." *Composites Part B: Engineering* 85: 76-92.
456 https://doi.org/10.1016/j.compositesb.2015.09.010.
457 GT. 2020. *Pretensioned centrifugal spun concrete piles with steel strands*. GT 47. Zhejiang: Zhejiang Standard
458 Design Station.
459 Huang, F. Y., S. W. Wu, X. Y. Luo, B. C. Chen, and Y. W. Lin. 2018. "Pseudo-static low cycle test on the
460 mechanical behavior of PHC pipe piles with consideration of soil-pile interaction." *Engineering Structures*
461 171: 992-1006. https://doi.org/10.1016/j.engstruct.2018.01.060.
462 Joen, P. H., and R. Park. 1990. "Flexural strength and ductility analysis of spirally reinforced prestressed
463 concrete piles." *PCI Journal* 35(4): 64-83. https://doi.org/10.15554/pcij.07011990.54.83.
464 JSCE (Japan Society of Civil Engineers). 2010. *JSCE guidelines for concrete no. 15: Standard specifications*
465 *for concrete structures - 2007 "Design"*. Tokyo: JSCE.

466 Kowalsky, M. J., M. J. N. Priestley, and G. A. Macrae. 1995. “Displacement-based design of RC bridge
467 columns in seismic regions.” *Earthquake Engineering and Structural Dynamics* 24(12): 1623-1643.
468 https://doi.org/10.1002/eqe.4290241206.
469 Lai, B. L., and J. Y. R. Liew. 2021. “Investigation on axial load-shorting behaviour of high strength concrete
470 encased steel composite section.” *Engineering Structures* 227: 111401.
471 https://doi.org/10.1016/j.engstruct.2020.111401.
472 Menegotto, M., and P. E. Pinto. 1973. “Method of analysis for cyclically loaded reinforced concrete plane
473 frame including changes in geometry and nonelastic behavior of elements under combined normal force and
474 bending.” In *Proceedings of IABSE symposium on resistance and ultimate deformability of structures acted*
475 *on by well-defined repeated loads*. Lisbon.
476 Nagae, T., and S. Hayashi. 2003. “Earthquake-resistant property of prefabricated high-strength concrete pile.”
477 In *Proceedings of the International Conference on High Performance Materials in Bridges*, 173-182. Kona,
478 Hawaii. https://doi.org/10.1061/40691(2003)16.
479 Nascimbene, R., and L. Bianco. 2021. “Cyclic response of column to foundation connections of reinforced
480 concrete precast structures: Numerical and experimental comparisons.” *Engineering Structures* 247: 113214.
481 https://doi.org/10.1016/j.engstruct.2021.113214.
482 Nascimbene, R. 2022. “Penalty partial reduced selective integration: a new method to solve locking
483 phenomena in thin shell steel and concrete structures.” *Curved and Layered Structures* 9: 352-364.
484 https://doi.org/10.1515/cls-2022-0027.
485 Park, R., and T. J. Falconer. 1983. “Ductility of prestressed concrete piles subjected to simulated seismic
486 loading.” *PCI Journal* 28: 112-144. https://doi.org/10.15554/pcij.09011983.112.144.
487 Ren, J. W., Q. B. Xu, G. Chen, C. B. Liu, S. F. Gong, and Y. Lu. 2021. “Flexural performance of pretensioned

488 centrifugal spun concrete piles with combined steel strands and reinforcing bars." *Structures* 34: 4467-4485.
489 https://doi.org/10.1016/j.istruc.2021.10.052.
490 Ren, J. W., Q. B. Xu, G. Chen, X. D. Yu, S. F. Gong, and Y. Lu. 2022. "Full-scale experimental study of the
491 seismic performance of pretensioned spun high-strength concrete piles." *Soil Dynamics and Earthquake*
492 *Engineering* 162: 107467. https://doi.org/10.1016/j.soildyn.2022.107467.
493 Ren, J. W., Q. B. Xu, G. Chen, X. D. Yu, S. F. Gong, and Y. Lu. 2023. "Seismic performance of pretensioned
494 centrifugal spun concrete piles with steel strands." *Structures* 50: 1303-1319.
495 https://doi.org/10.1016/j.istruc.2023.02.107.
496 Roeder, C. W., R. Graff, J. Soderstrom, and J. H. Yoo. 2005. "Seismic performance of pile-wharf connections."
497 *Journal of Structural Engineering* 131(3): 428-437. https://doi.org/10.1061/(ASCE)0733-
498 9445(2005)131:3(428).
499 Silva, P. F., F. Seible, and M. J. N. Priestley. 2001. "Influence of strand development length in formation of
500 plastic hinges in prestressed piles." *PCI Journal* 46(3): 76-89. https://doi.org/10.15554/pcij.05012001.76.89.
501 Tao, Y. C., W. J. Zhao, J. P. Shu, and Y. Z. Yang. 2021. "Nonlinear finite-element analysis of the seismic
502 behavior of RC column-steel beam connections with shear failure mode." *Journal of Structural Engineering*
503 147(10): 04021160. https://doi.org/10.1061/(ASCE)ST.1943-541X.0003132.
504 Thusoo, S., T. Obara, S. Kono, and K. Miyahara. 2021. "Design models for steel encased high-strength precast
505 concrete piles under axial-flexural loads." *Engineering Structures* 228: 111465.
506 https://doi.org/10.1016/j.engstruct.2020.111465.
507 TNO (Thai National Observatory). 2020. *Diana finite element analysis, user's manual—Release 10.4*. Delft,
508 Netherlands: TNO.
509 Tong, T., W. D. Zhuo, X. F. Jiang, H. P. Lei, and Z. Liu. 2019. "Research on seismic resilience of prestressed

precast segmental bridge piers reinforced with high-strength bars through experimental testing and numerical modelling." *Engineering Structures* 197: 109335. https://doi.org/10.1016/j.engstruct.2019.109335.

Uzuoka, R., N. Sento, M. Kazama, F. Zhang, A. Yashima, and F. Oka. 2007. "Three-dimensional numerical simulation of earthquake damage to group-piles in a liquefied ground." *Soil Dynamics and Earthquake Engineering* 27: 395-413. https://doi.org/10.1016/j.soildyn.2006.10.003.

Wang, P., J. Huang, Y. Tao, Q. X. Shi, and C. Rong. 2022. "Seismic performance of reinforced concrete columns with an assembled UHPC stay-in-place formwork." *Engineering Structures* 272: 115003. https://doi.org/10.1016/j.engstruct.2022.115003.

Wang, W. D., C. W. W. Ng, Y. Hong, Y. Hu, and Q. Li. 2019. "Forensic study on the collapse of a high-rise building in Shanghai: 3D centrifuge and numerical modelling." *Géotechnique* 69: 847-862. https://doi.org/10.1680/jgeot.16.P.315.

Yang, Z. J., G. C. Li, W. J. Wang, and Y. J. Lv. 2018. "Study on the flexural performance of prestressed high strength concrete pile." *KSCE Journal of Civil Engineering* 22(10): 4073-4082. https://doi.org/10.1007/s12205-018-1811-y.

Zhang, X. W., S. F. Gong, Q. B. Xu, G. Gan, X. D. Yu, and Y. Lu. 2022. "Flexural performance of pretensioned spun concrete piles reinforced with steel strands." *Magazine of Concrete Research* 74(15): 757-777. https://doi.org/10.1680/jmacr.21.00146.

Zhang, X. Z., S. H. Zhang, S. B. Xu, and S. X. Niu. 2020. "Study of seismic behavior of PHC piles with partial normal-strength deformed bars." *Earthquake Engineering and Engineering Vibration* 19(2): 307–320. https://doi.org/10.1007/s11803-020-0563-0.

Table 1. Geometric dimensions and reinforcement of PSRC piles and PSC piles

Specimen	D (mm)	D_p (mm)	t (mm)	Longitudinal reinforcement	ρ_s (%)	Stirrup	σ_{con} (MPa)	P/Af_{cd}
PSRC-1	500	406	100	$11\Phi^S11.1$+11D16	0.65+1.76	$\Phi^{RH}5$@45	1302	0
PSRC-2	500	406	100	$11\Phi^S11.1$+11D16	0.65+1.76	$\Phi^{RH}5$@45	1302	0.2
PSRC-3	500	406	100	$11\Phi^S11.1$+11D16	0.65+1.76	$\Phi^{RH}5$@45	1302	0.4
PSC-1	500	406	100	$11\Phi^S11.1$	0.65	$\Phi^{RH}5$@45	1302	0
PSC-2	500	406	100	$11\Phi^S11.1$	0.65	$\Phi^{RH}5$@45	1302	0.2
PSC-3	500	406	100	$11\Phi^S11.1$	0.65	$\Phi^{RH}5$@45	1302	0.4

Note: D denotes diameter of pile. D_p denotes diameter of distribution circle of longitudinal reinforcement. t denotes wall thickness of pile. ρ_s denotes longitudinal reinforcement ratio.

Table 2. Material mechanical parameters of reinforcements

Reinforcement	E_s (GPa)	f_y (MPa)	f_u (MPa)	A_{gt} (%)
Φ^S11.1 HSS	195	1725	1920	6.4
D16 HRB	193	504	615	11.2
Φ^{RH}5 CRB	205	616	643	6.0

Note: HSS denotes high-strength steel strand (prestressing tendon). HRB denotes hot-rolled ribbed bar (non-prestressing deformed steel bar). CRB denotes cold-rolled ribbed bar (stirrup).

Table 3. Main parameters of specimens

Specimen	Load direction	Crack	Yield		Peak		Ultimate	μ_θ
		M_{cr} (kN·m)	M_y (kN·m)	θ_y (%)	M_{max} (kN·m)	θ_{max} (%)	θ_u (%)	
PSRC-1	(+)	174.3	445.5	1.44	527.1	2.95	5.68	3.95
	(−)	178.1	437.9	1.72	506.5	2.94	6.11	3.56
PSRC-2	(+)	318.1	611.2	1.17	723.2	1.91	3.81	3.25
	(−)	253.3	528.5	1.24	615.3	1.90	4.70	3.78
PSRC-3	(+)	346.1	661.7	0.91	784.7	1.60	3.10	3.40
	(−)	360.8	679.1	0.93	804.4	1.60	2.96	3.18
PSC-1	(+)	177.7	308.2	0.89	367.9	2.26	4.33	4.85
	(−)	168.9	288.7	1.05	340.9	2.63	4.39	4.20
PSC-2	(+)	290.6	489.2	0.85	593.9	1.57	2.70	3.16
	(−)	272.2	429.0	0.78	514.3	1.52	2.78	3.57
PSC-3	(+)	340.0	504.2	0.78	595.4	1.33	1.78	2.30
	(−)	420.3	617.4	0.86	726.9	1.53	1.92	2.23

Click here to access/download;Figure;Fig 1.pdf

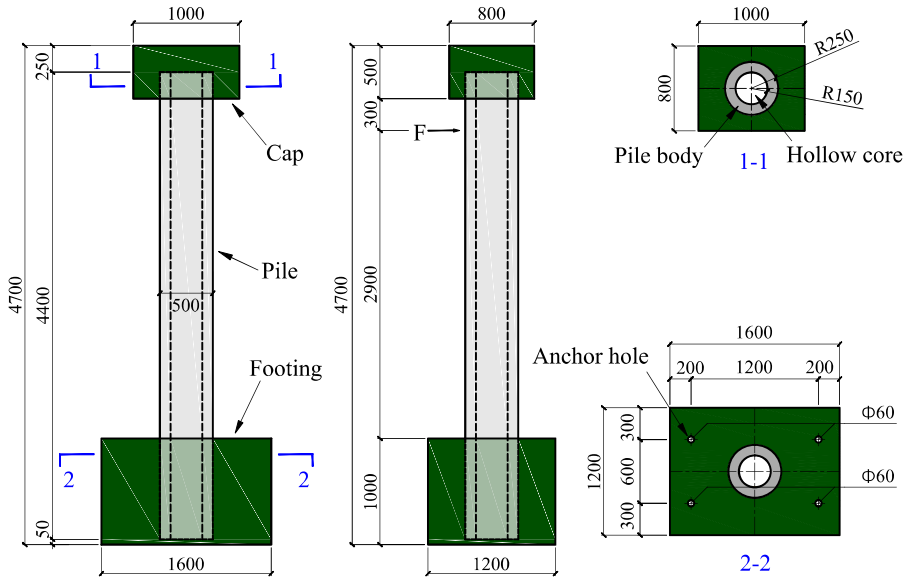

Fig. 1. Dimensions of pile specimens.

Click here to access/download;Figure;Fig 2.pdf

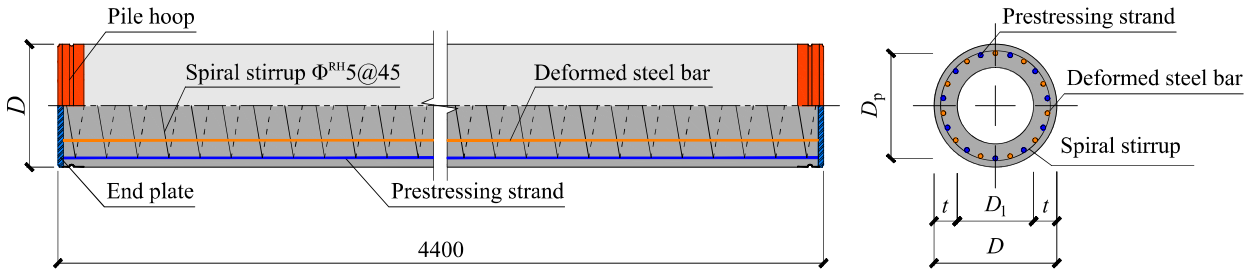

Fig. 2. Schematic diagram of reinforcement in PSRC piles.

Click here to access/download;Figure;Fig 3.pdf

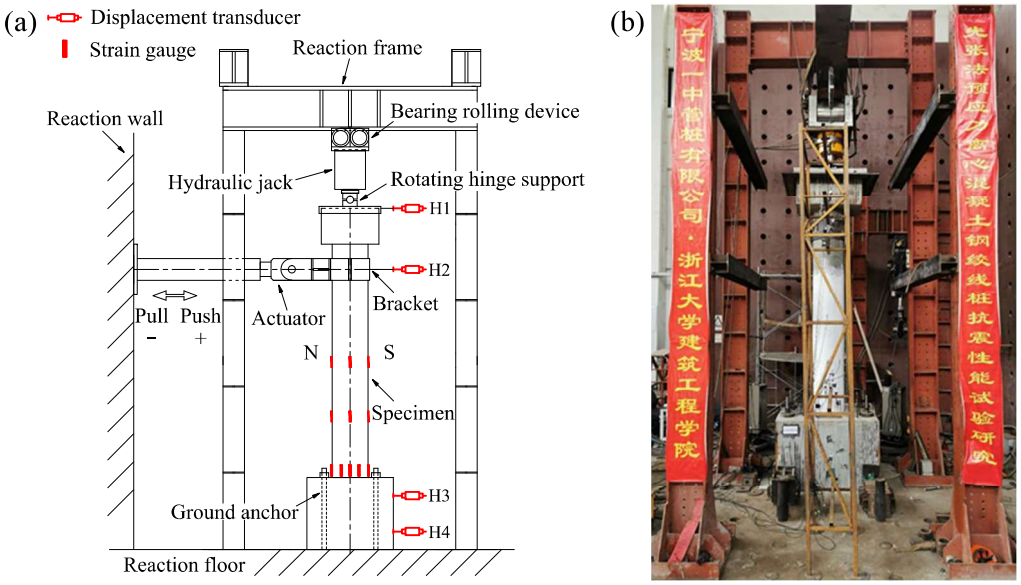

Fig. 3. Test setup: (a) Schematic diagram of setup; and (b) Setup photo. (Image by Junwei Ren.)

Click here to access/download;Figure;Fig 4.pdf

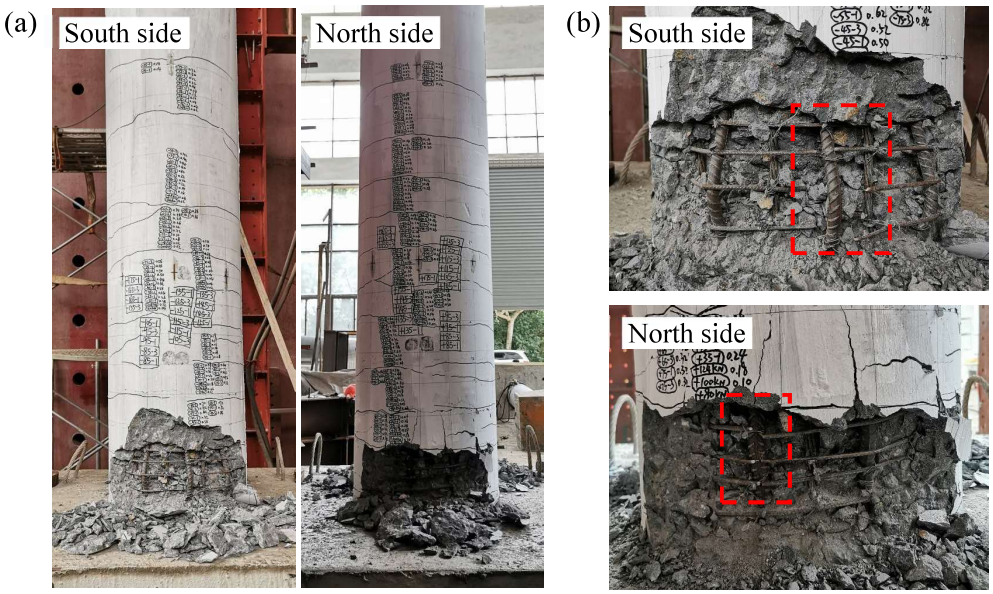

Fig. 4. Failure patterns of PSRC-1: (a) Overall view; and (b) Detail view. (Images by Junwei Ren.)

Click here to access/download;Figure;Fig 5.pdf

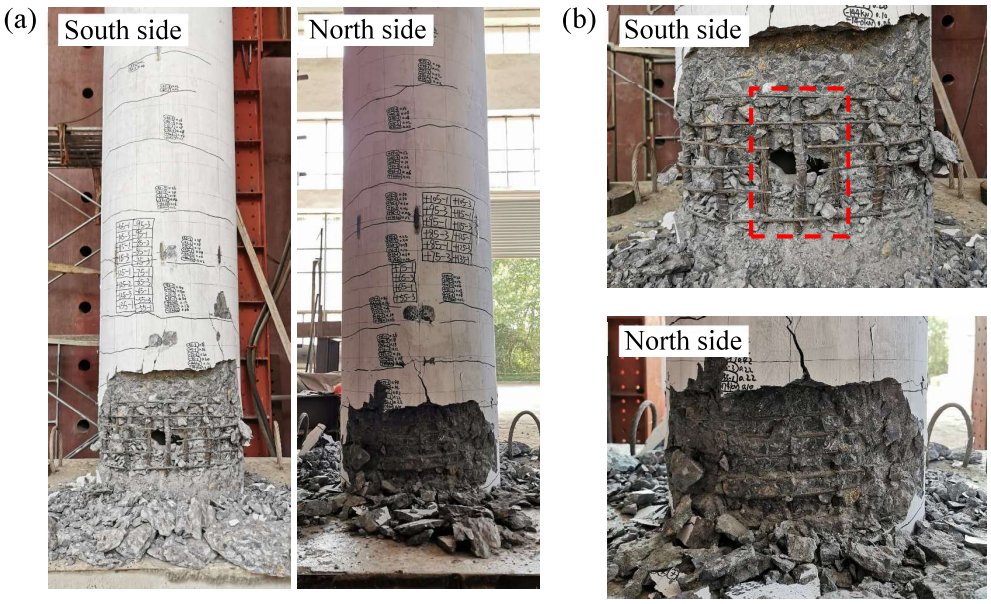

Fig. 5. Failure patterns of PSRC-2: (a) Overall view; and (b) Detail view. (Images by Junwei Ren.)

Click here to access/download;Figure;Fig 6.pdf

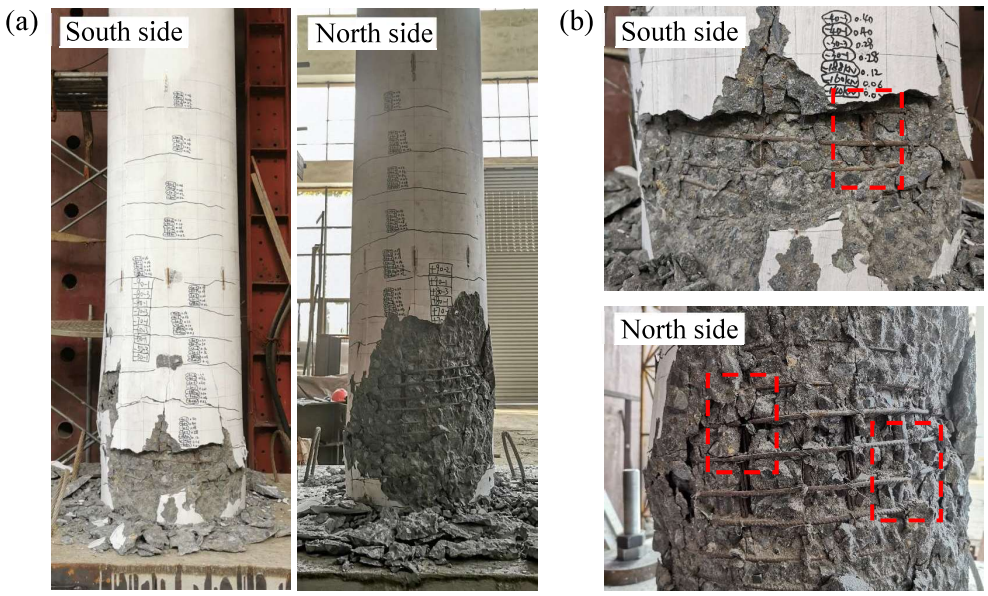

Fig. 6. Failure patterns of PSRC-3: (a) Overall view; and (b) Detail view. (Images by Junwei Ren.)

Click here to access/download;Figure;Fig 7.pdf

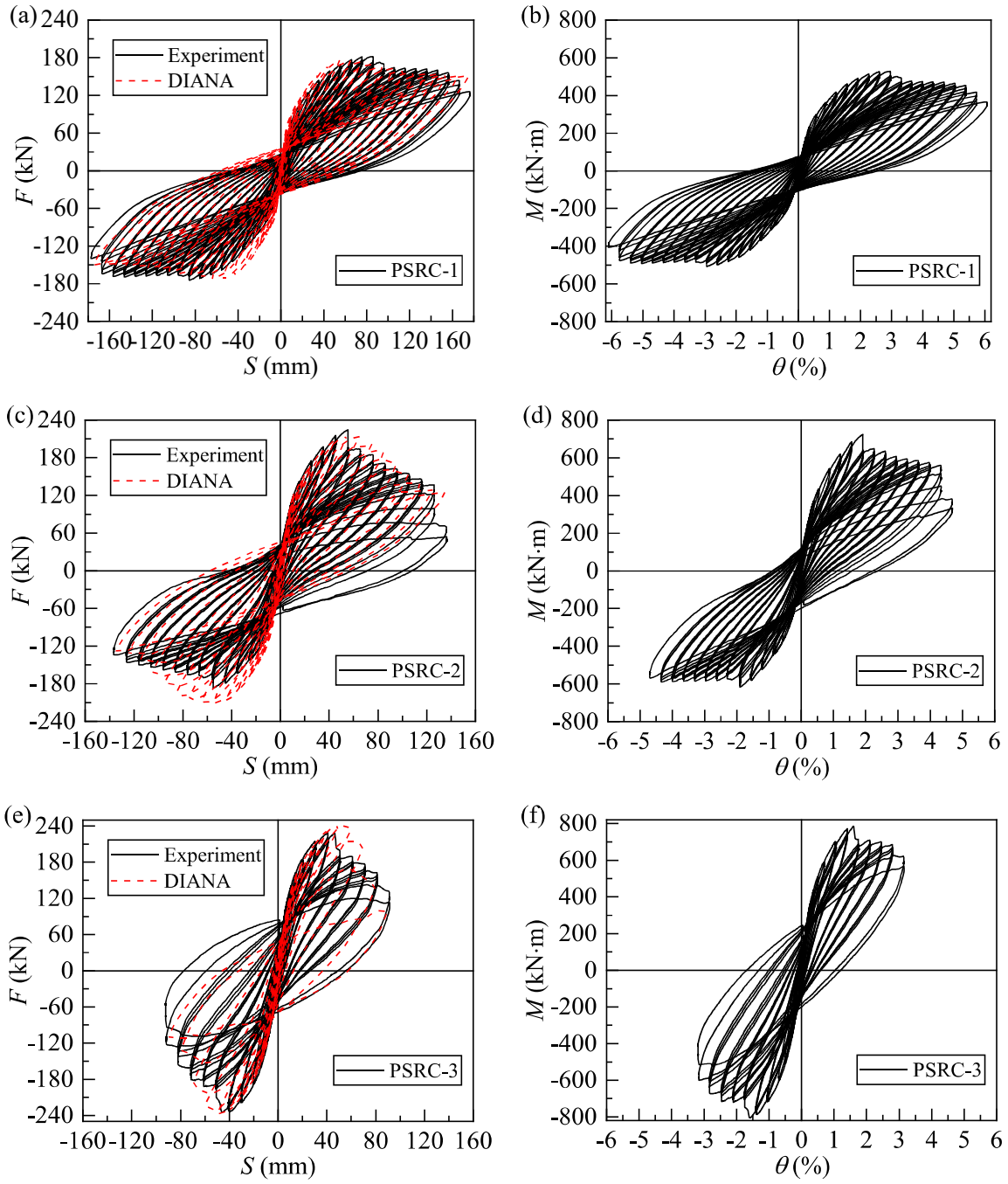

Fig. 7. Hysteretic curves for specimens: (a) *F*-*S* for PSRC-1; (b) *M*-*θ* for PSRC-1; (c) *F*-*S* for PSRC-2; (d) *M*-*θ* for PSRC-2; (e) *F*-*S* for PSRC-3; and (f) *M*-*θ* for PSRC-3.

Click here to access/download;Figure;Fig 8.pdf

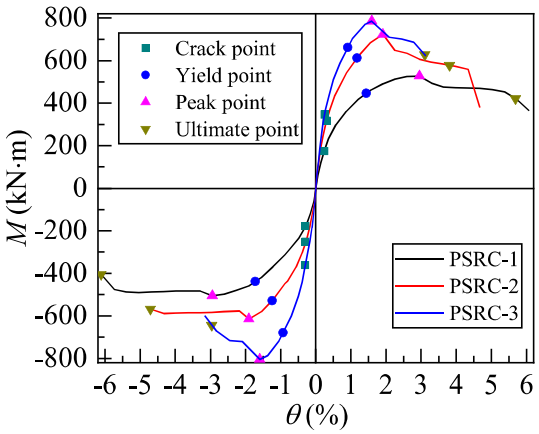

Fig. 8. Backbone curves of M-θ for specimens.

Click here to access/download;Figure;Fig 9.pdf

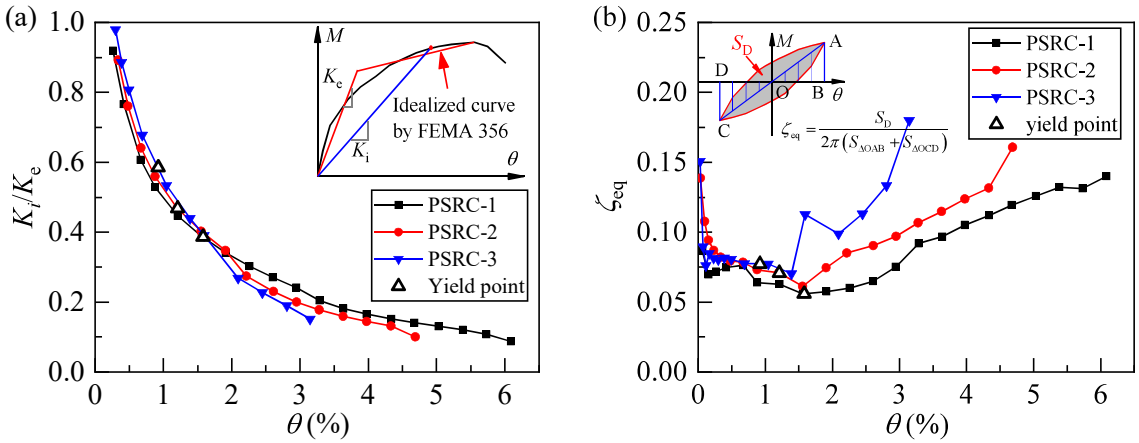

Fig. 9. (a) Stiffness degradation of specimens; and (b) Equivalent viscous damping ratio of specimens.

Click here to access/download;Figure;Fig 10.pdf

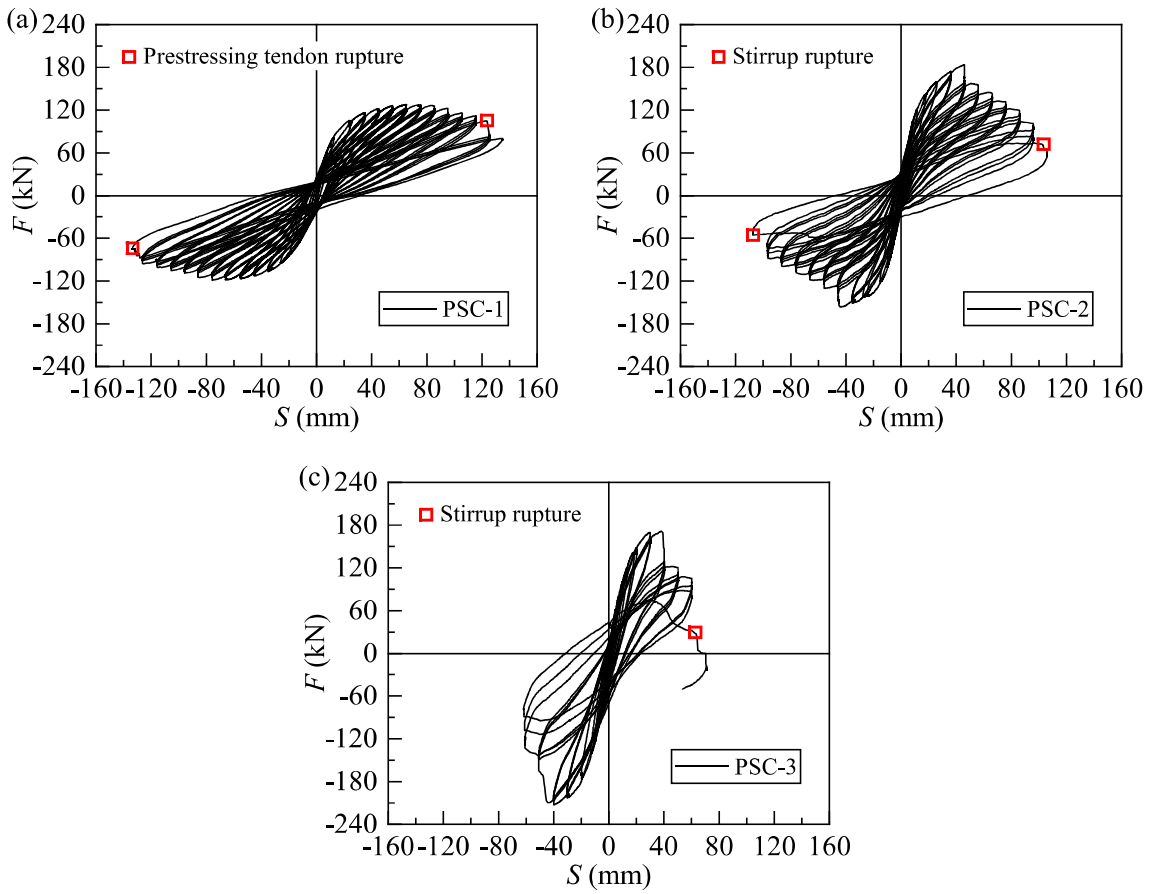

Fig. 10. Hysteretic curves for (a) PSC-1; (b) PSC-2; and (c) PSC-3 specimens, to be compared with PSRC specimens shown in Fig. 7.

Click here to access/download;Figure;Fig 11.pdf

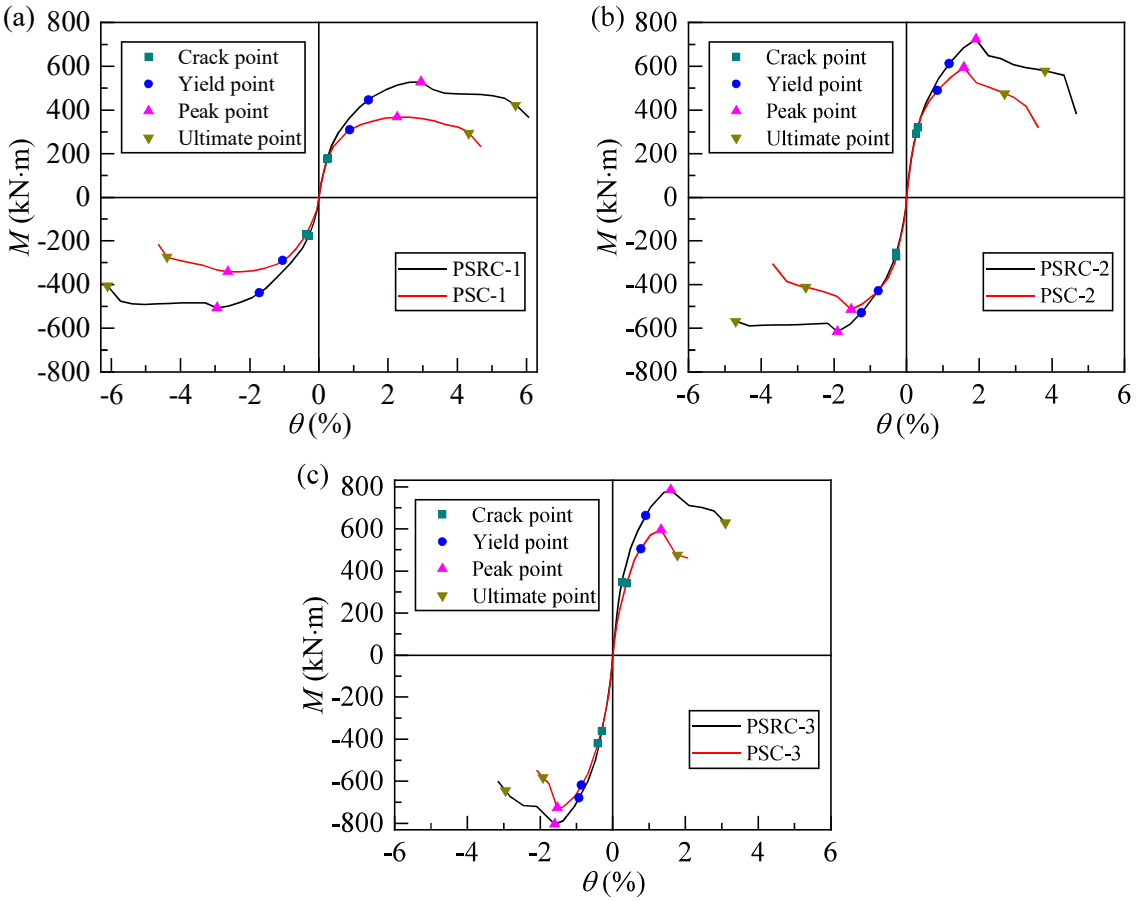

Fig. 11. Comparison of backbone curves between PSRC piles and PSC piles: (a) 0 axial force ratio; (b) 0.2 axial force ratio; and (c) 0.4 axial force ratio.

Click here to access/download;Figure;Fig 12.pdf

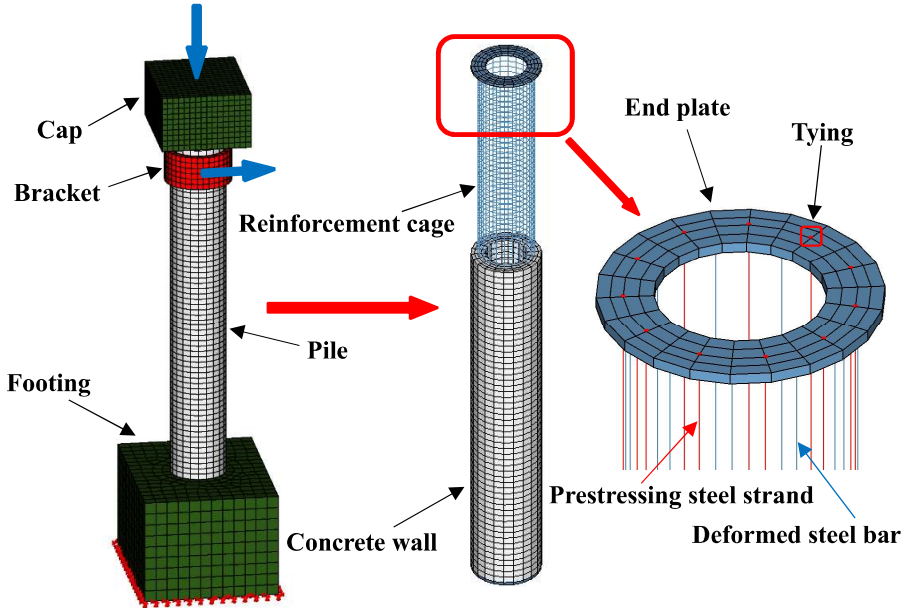

Fig. 12. FE model of PSRC pile specimens.

Click here to access/download;Figure;Fig 13.pdf

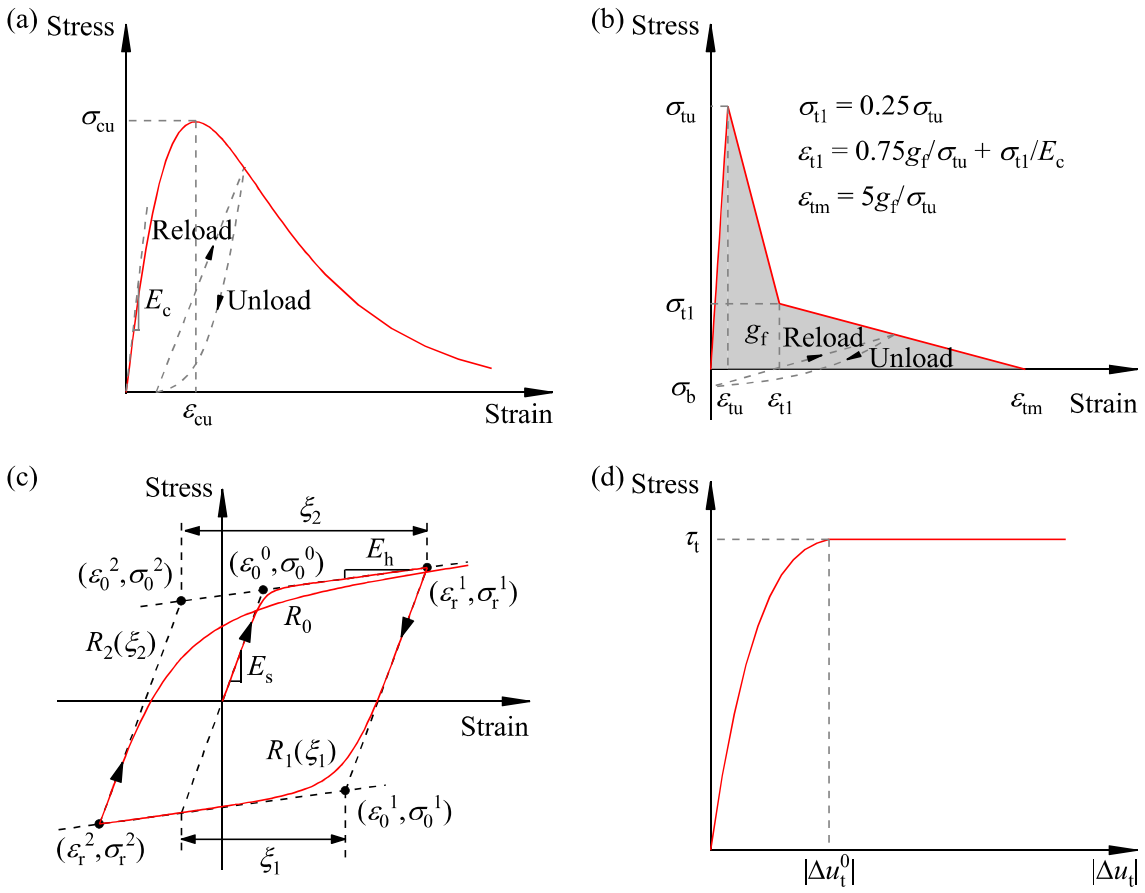

Fig. 13. Constitutive models: (a) Concrete in compression; (b) Concrete in tension; (c) Material model of reinforcements; and (d) Bond-slip model.

Click here to access/download;Figure;Fig 14.pdf

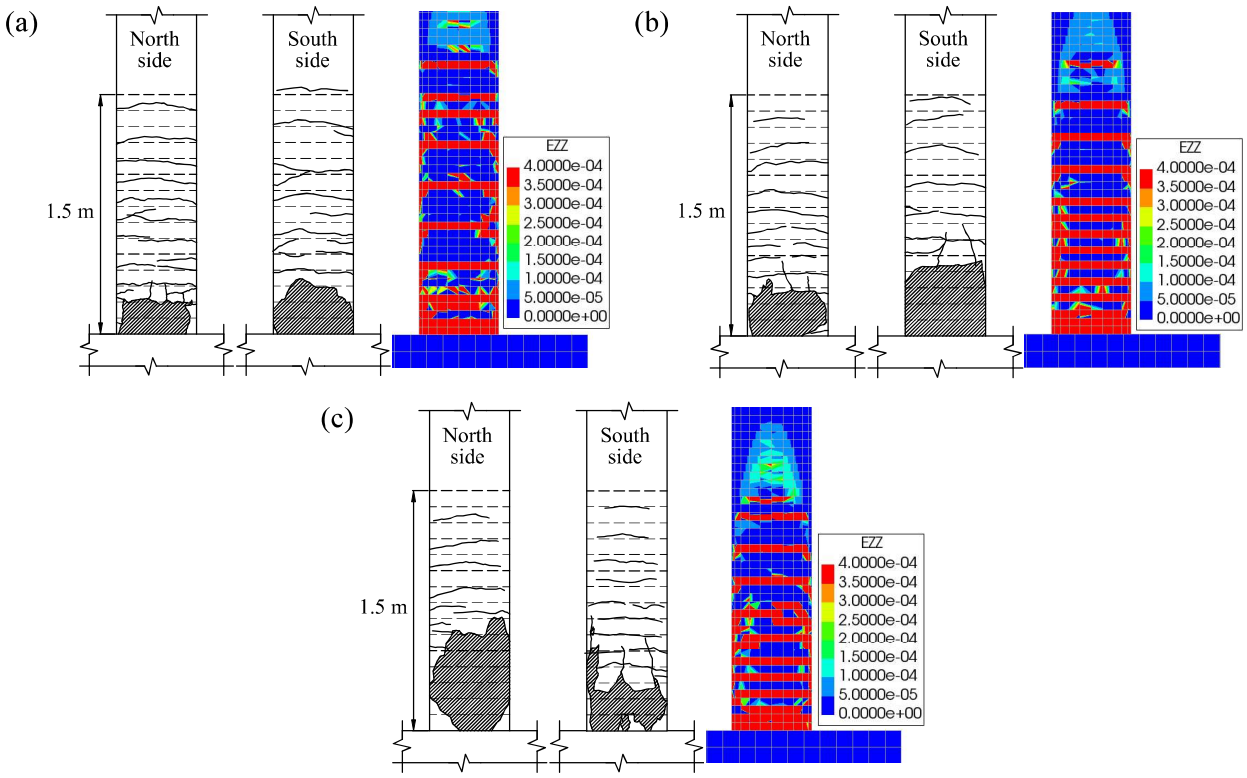

Fig. 14. Crack pattern of experimental and numerical results for test specimens: (a) PSRC-1; (b) PSRC-2; and (c) PSRC-3.

Click here to access/download;Figure;Fig 15.pdf

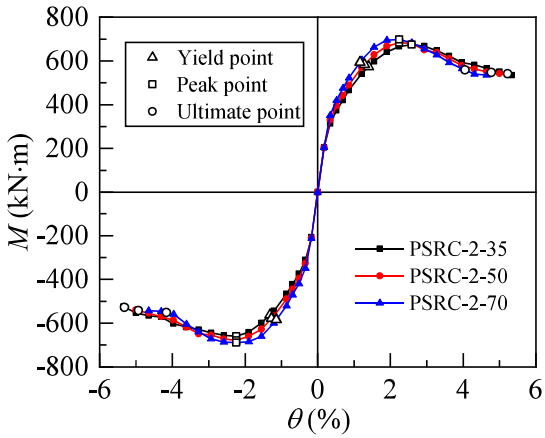

Fig. 15. Backbone curves of FE model specimens with different prestressing levels of HSSs.

Click here to access/download;Figure;Fig 16.pdf

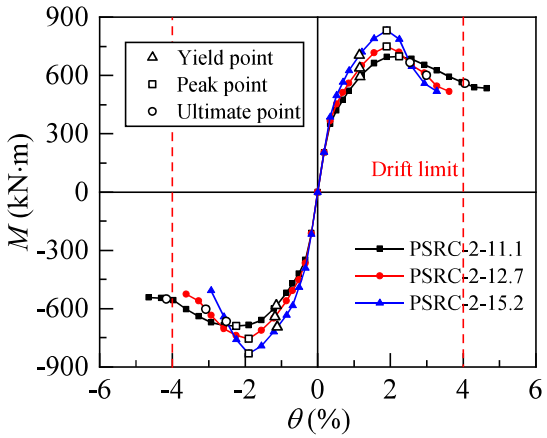

Fig. 16. Backbone curves of FE model specimens with different prestressing tendon HSS ratios.

Click here to access/download;Figure;Fig 17.pdf

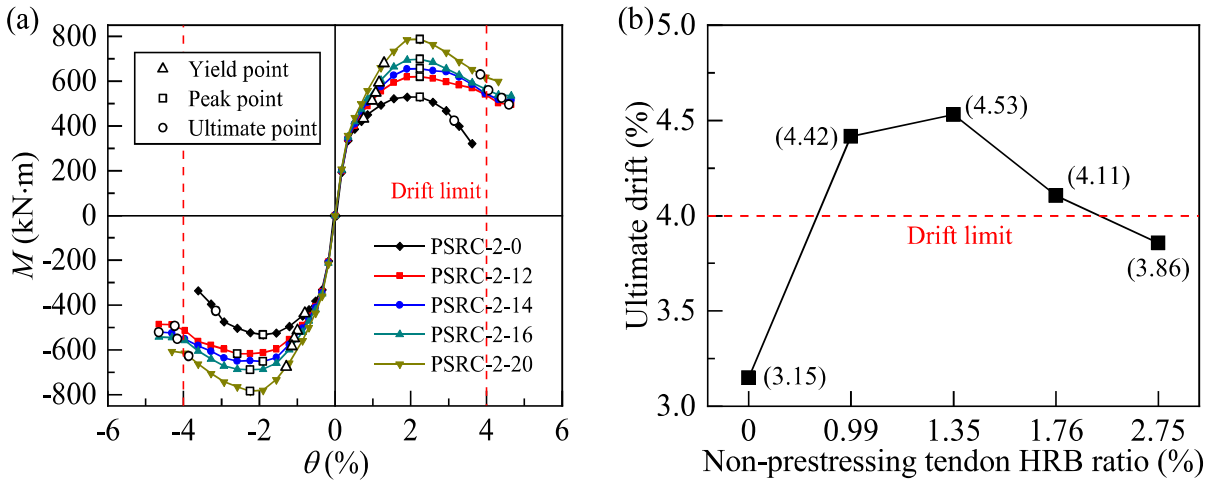

Fig. 17. (a) Backbone curves of FE model specimens with different non-prestressing HRB ratios; and (b) Ultimate drift vs. HRB ratio in FE model specimens.

Click here to access/download;Figure;Fig 18.pdf

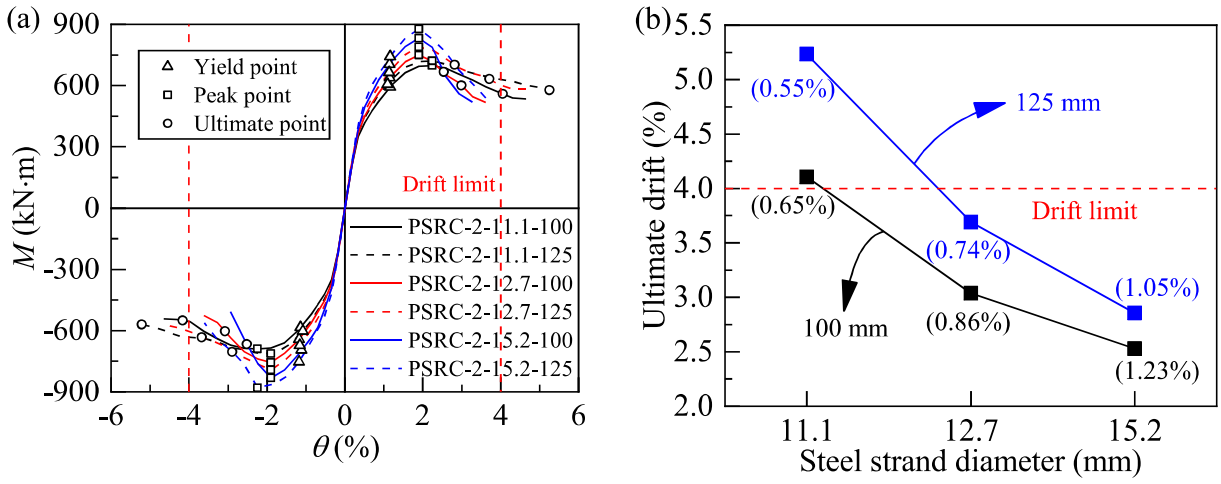

Fig. 18. (a) Backbone curves of FE model specimens with different concrete wall thicknesses; and (b) Ultimate drift vs. steel strand diameter in FE model specimens.

List of Figure Captions

Fig. 16. Backbone curves of FE model specimens with different prestressing tendon HSS ratios.

Fig. 17. (a) Backbone curves of FE model specimens with different non-prestressing HRB ratios; and (b) Ultimate drift vs. HRB ratio in FE model specimens.

Fig. 18. (a) Backbone curves of FE model specimens with different concrete wall thicknesses; and (b) Ultimate drift vs. steel strand diameter in FE model specimens.